Supplement of Atmos. Chem. Phys., 26, 15523–15542, 2026
https://doi.org/10.5194/acp-26-15523-2026-supplement
© Author(s) 2026. CC BY 4.0 License.



Atmospheric Chemistry and Physics
Open Access
EGU

Supplement of

Impacts of synoptic circulation types on nocturnal ozone increase in the North China Plain: meteorological drivers and physical mechanisms

Huanpeng Wang et al.

Correspondence to: Liya Fan (fanly@scut.edu.cn)

The copyright of individual parts of the supplement might differ from the article licence.

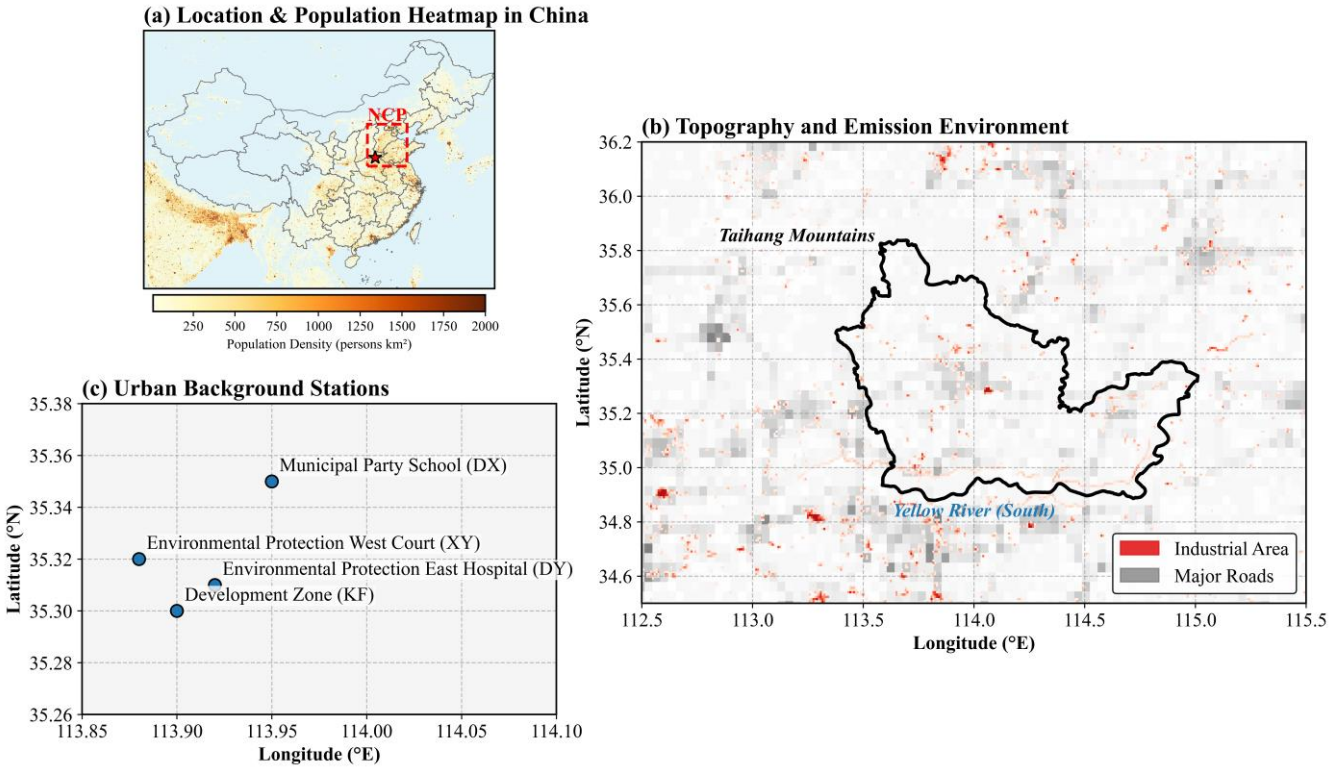


Figure S1: Geographical setting, regional emission context, and spatial distribution of monitoring stations. (a) Location of the study area within China, superimposed on the gridded population density distribution. The red dashed rectangle delineates the North China Plain (NCP), and the red star marks the geographical location of Xinxiang. (b) Multi-source emission environment across Xinxiang. Spatial layers depict major industrial area (red) and major roads (dark grey), with the black solid boundary indicating the municipal boundary of Xinxiang. (c) Spatial arrangement of the national air quality monitoring stations (KF (Development Zone), DY (Environmental Protection East Hospital), XY (Environmental Protection West Court), and DX (Municipal Party School)) located in the urban core of Xinxiang. The spatial distribution data for population density, industrial area, and major roads are derived from Wang et al. (2024a).

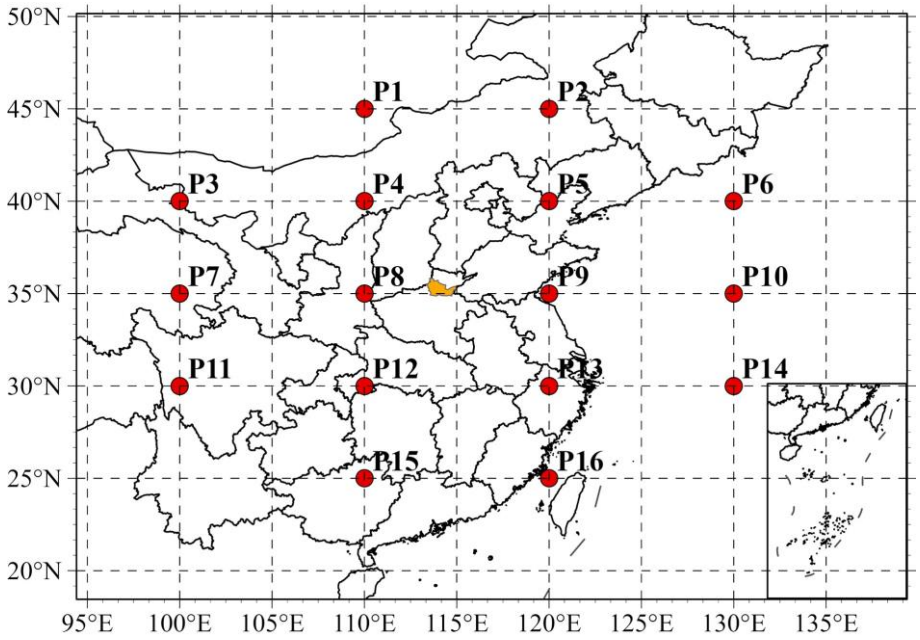


Figure S2: Lamb-Jenkinson synoptic circulation classification grid diagram (P1-P16 are the 16 grid points selected, and the orange area is Xinxiang).

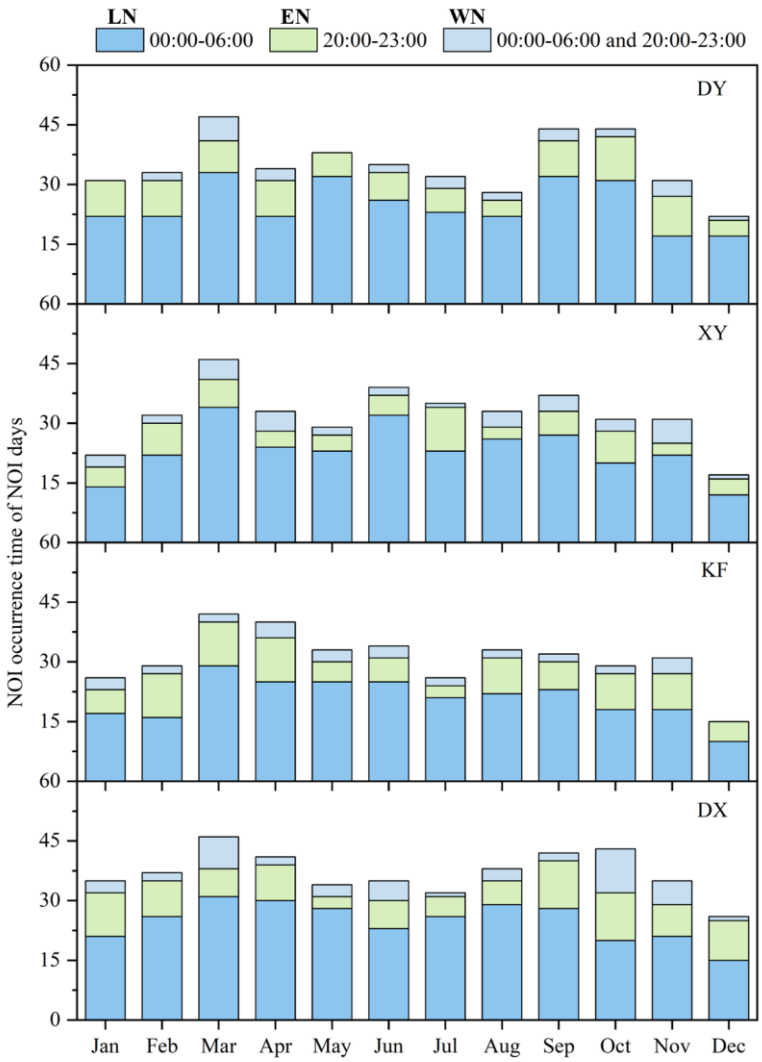


Figure S3: Monthly variation of NOI occurrence time at national monitoring stations in Xinxiang, 2021-2023. The abbreviations (EN, LN and WN) represent three distinct temporal categories of NOI days: Early-night (EN, 20:00-23:00 LT), Late-night (LN, 00:00-06:00 LT), and Whole-night (WN, events persisting continuously across both EN and LN periods).

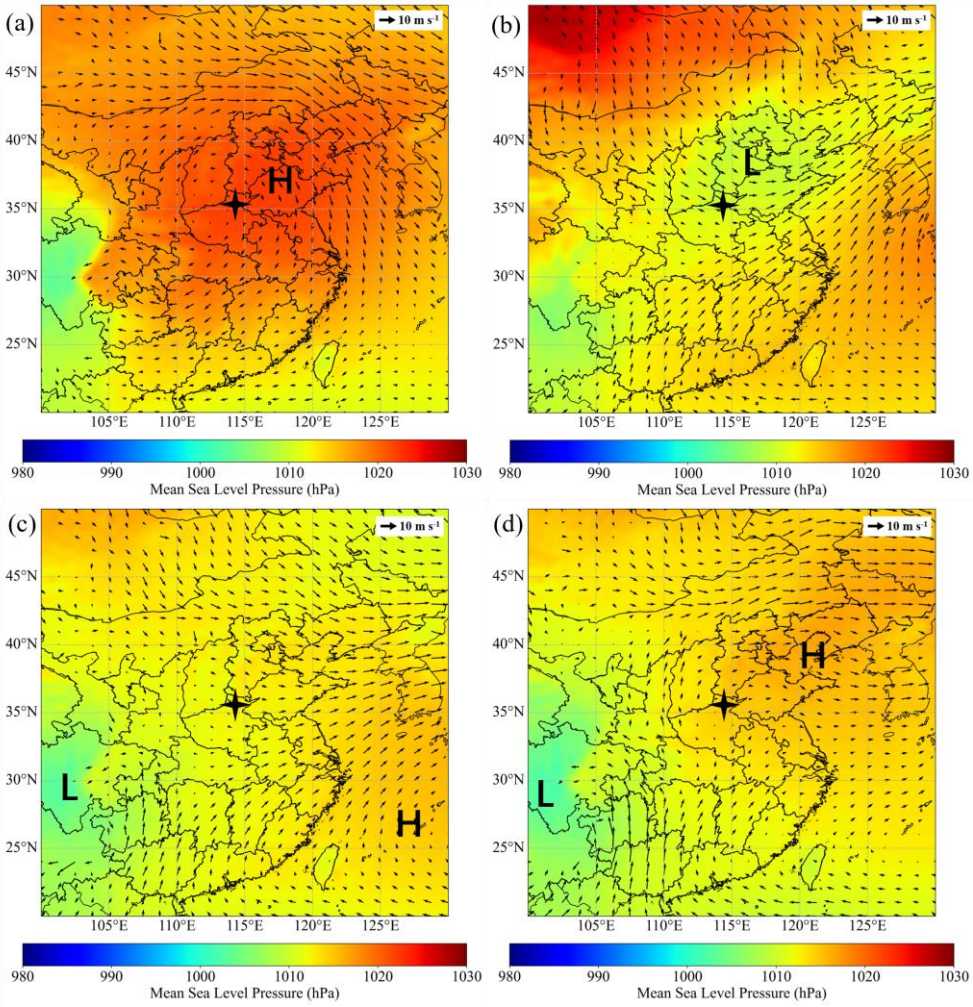


Figure S4: Spatial distribution of composite mean SLP and 850 hPa wind fields under different weather types for representative NOI days: (a) vorticity type A, (b) vorticity type C, (c) direction types, (d) hybrid types (asterisk indicates the location of Xinxiang; "H" and "L" stand for high-pressure and low-pressure, respectively).

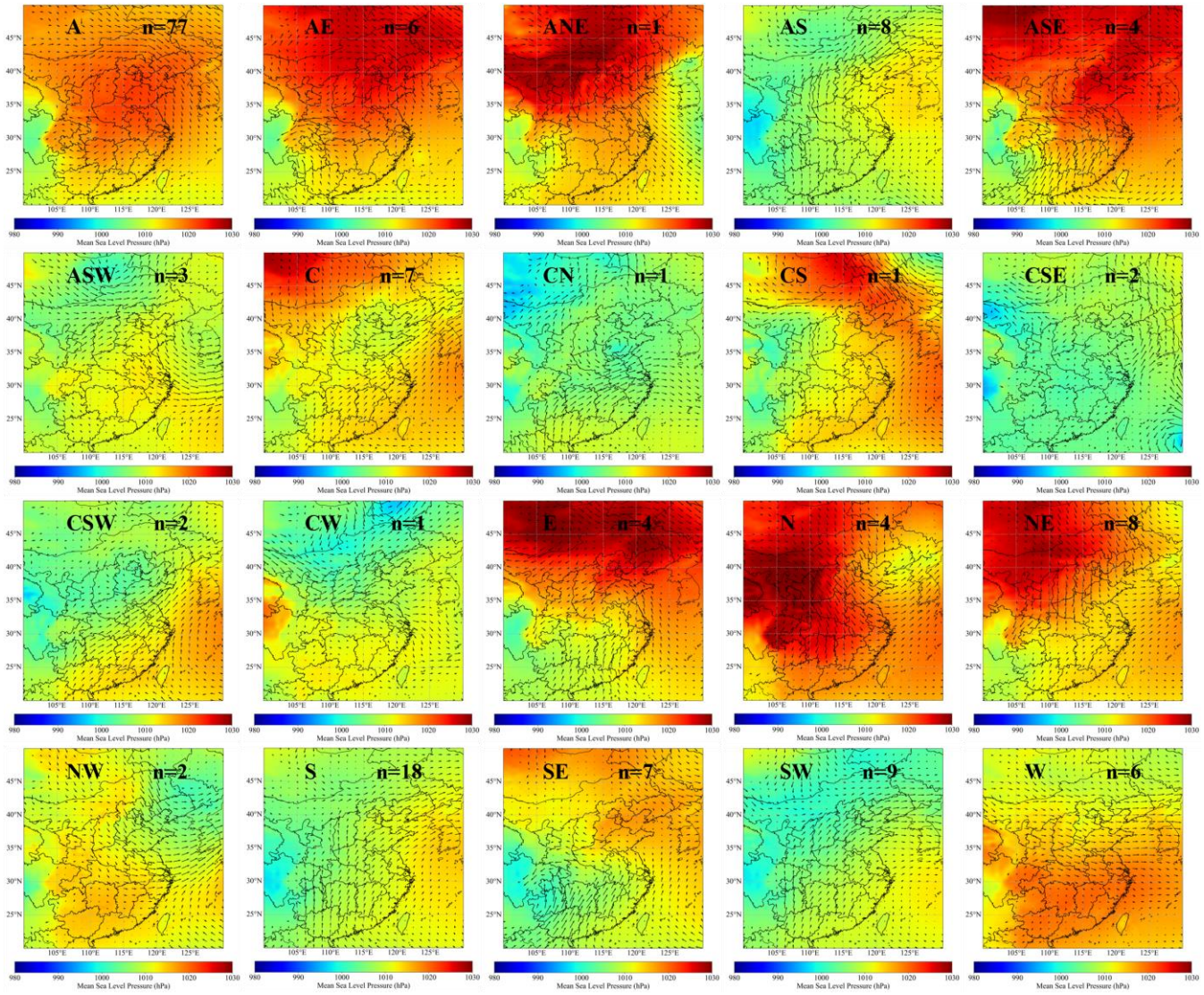


Figure S5: Spatial distribution of composite mean SLP and 850 hPa wind fields under different weather types (Preliminarily identified based on the Lamb-Jenkinson synoptic circulation classification method; n denotes the number of days).

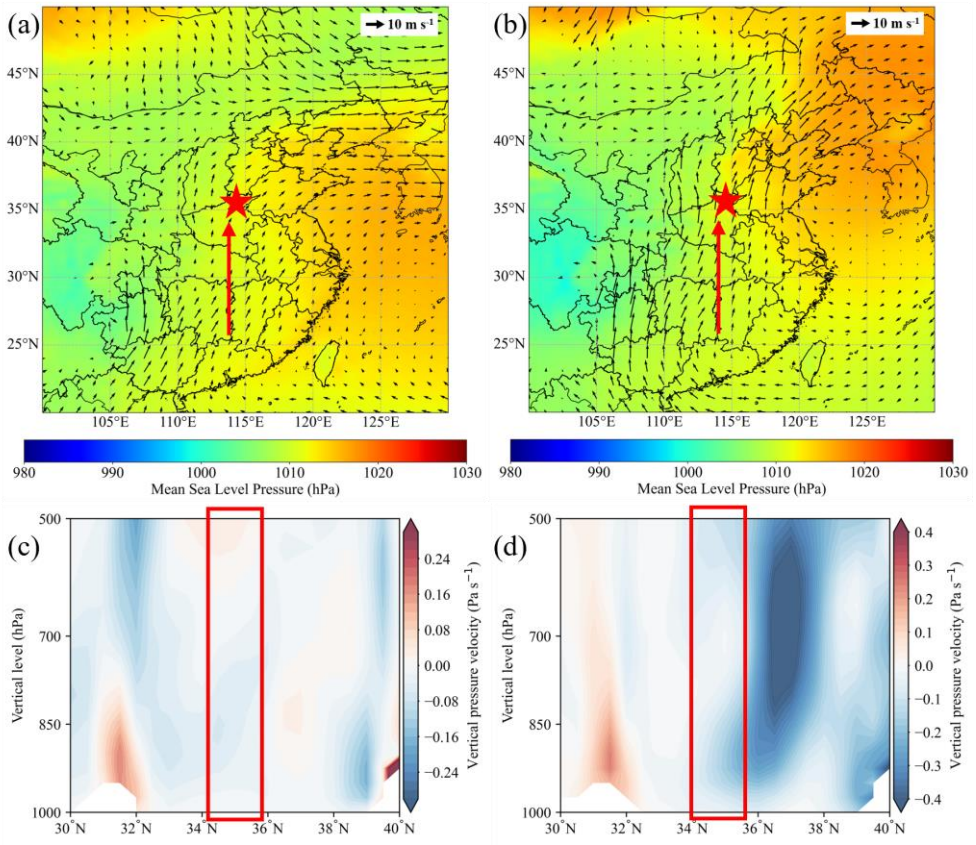


Figure S6: During spring ((a) and (c)) and autumn ((b) and (d)), spatial distribution of composite mean SLP and 850 hPa wind fields ((a) and (b)), and vertical profiles of pressure velocity ((c) and (d)) under S-type (asterisk indicates the location of Xinxiang; red rectangles indicate the region of Xinxiang). In terms of vertical pressure velocity, negative values correspond to upward motion, while positive values indicate subsidence.

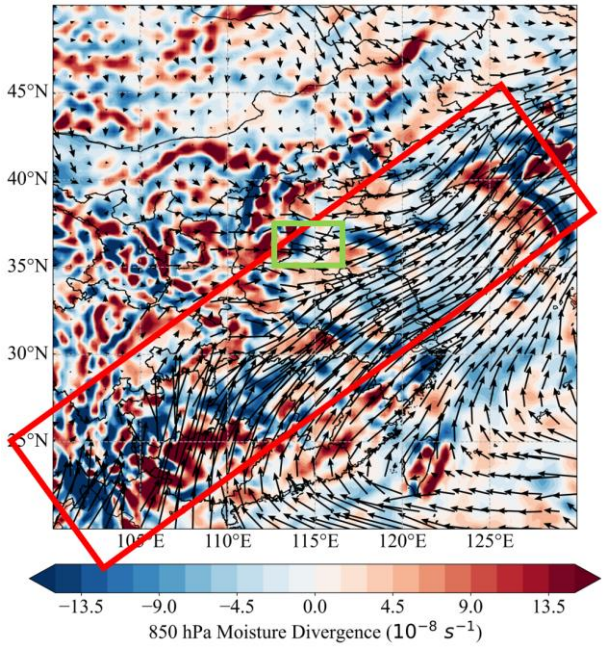


Figure S7: 850 hPa water vapor flux and divergence fields under C-type (the red box denotes the moisture transport path, corresponding to Fig. 5(b); the green box marks the Xinxiang region).

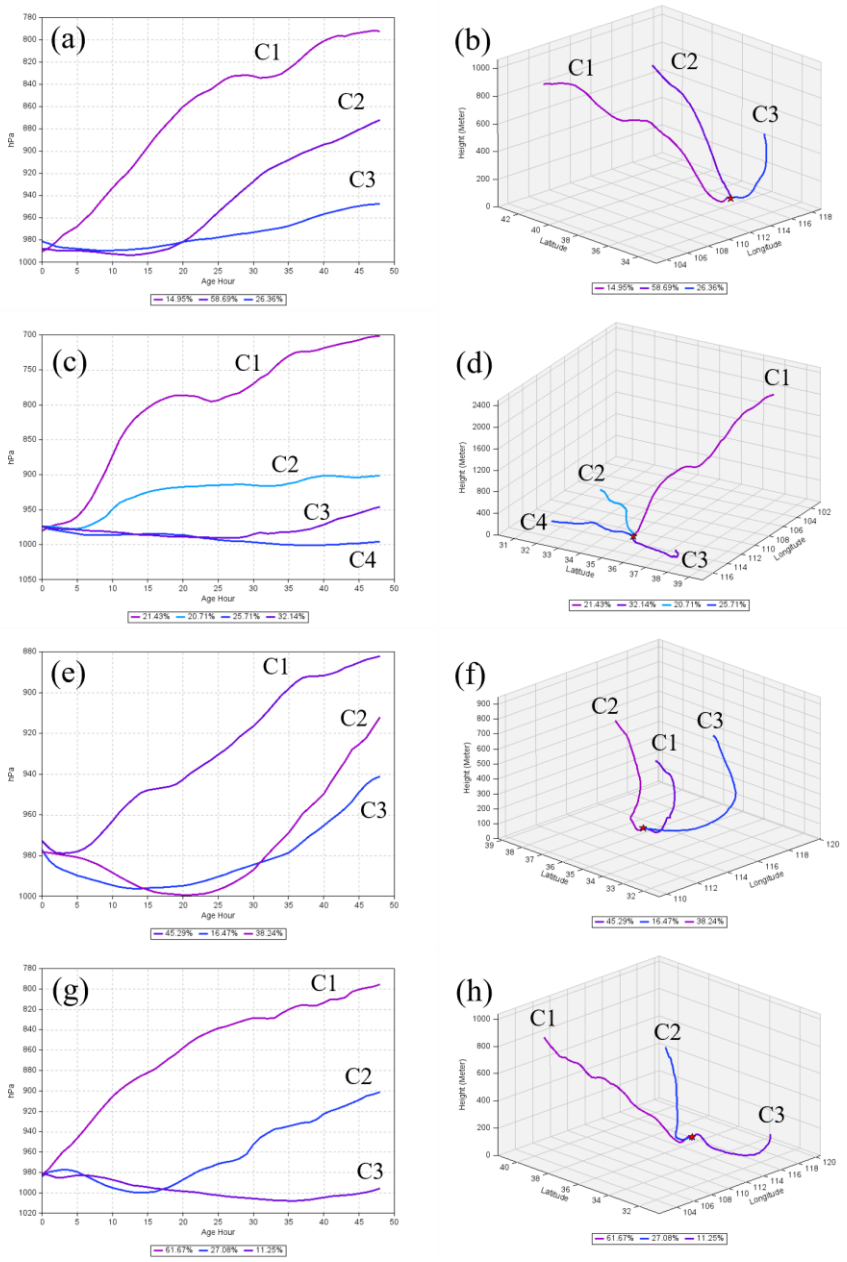


Figure S8: 3D clustered backward trajectories and their corresponding vertical pressure profiles for air masses arriving at Xinxiang under the four weather types. The left column (a), (c), (e), (g) displays the altitude-time cross-sections (represented by atmospheric pressure, hPa) of the trajectory clusters over the 48-hour backward tracking period. The right column (b), (d), (f), (h) illustrates the 3D spatial pathways of these clusters. The four rows from top to bottom correspond to A-type (a, b), C-type (c, d), S-type (e, f), and WNE-type (g, h), respectively. The red star denotes the receptor site (Xinxiang). The percentages in the legends indicate the relative contribution of each trajectory cluster to the total trajectories under that specific weather type. To facilitate a direct and clear comparison between the temporal-altitude profiles (left column) and the spatial pathways (right column), explicit corresponding markers (e.g., C1, C2, C3) have been added next to each paired trajectory cluster in both panels.

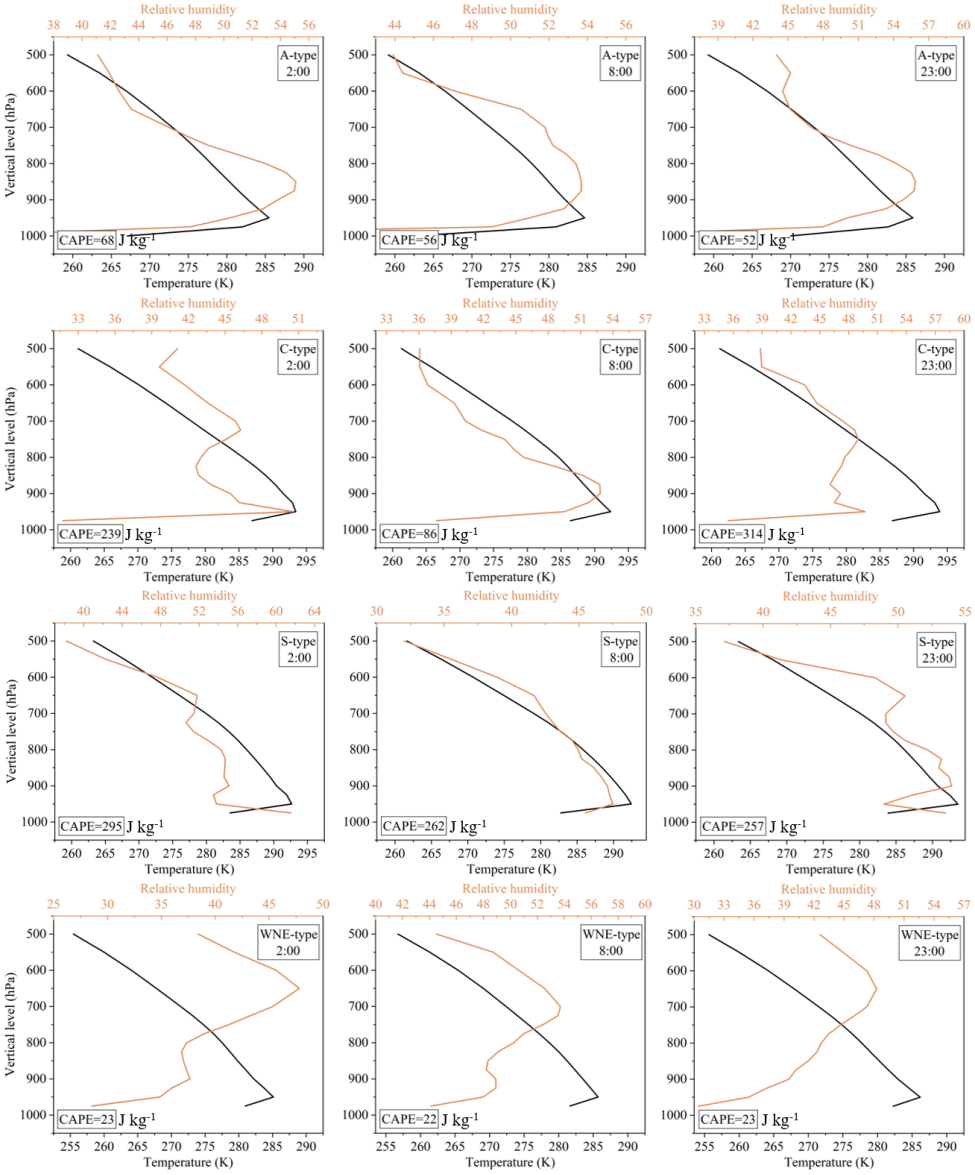


Figure S9: Vertical profiles of temperature (solid black lines, K) and relative humidity (solid orange lines, %) over Xinxiang under the four weather types (A, C, S, and WNE). The three columns from left to right display the vertical atmospheric structure at specific diurnal hours (02:00, 08:00, and 23:00 LT, respectively). The Convective Available Potential Energy (CAPE) values are indicated in the bottom-left corner of each panel, with units in J kg^{-1}. Vertical profiles of temperature and relative humidity are derived from MERRA-2. CAPE data is derived from ERA5.

Table S1. Weather classification results of representative NOI days in Xinxiang, 2021-2023.

	Weather type	2021	2022	2023	Total	Percentage
Vorticity types	A	26	25	26	77	49.12%
	C	2	3	2	7	
Directional types	S	5	11	2	18	33.92%
	SE	5	1	1	7	
	SW	4	2	3	9	
	W	4	1	1	6	
	NW	0	2	0	2	
	N	1	0	3	4	
	NE	2	2	4	8	
	E	2	1	1	4	
Hyrid types	AE	2	3	1	6	16.96%
	ANE	1	0	0	1	
	AS	2	4	2	8	
	ASE	2	1	1	4	
	ASW	0	0	3	3	
	CN	0	1	0	1	
	CS	0	1	0	1	
	CSE	0	1	1	2	
	CSW	2	0	0	2	
	CW	0	0	1	1	

Table S2. Statistical summary of nocturnal meteorological anomalies and ANOVA results under the four weather types.

Variable	A-type	C-type	S-type	WNE-type	p-value
ΔT (℃)	-1.07 ± 3.41	2.60 ± 3.54	1.06 ± 3.18	0.77 ± 3.70	< 0.01**
ΔRH (%)	-0.31 ± 14.82	4.08 ± 14.00	-7.12 ± 20.46	-11.15 ± 20.72	< 0.01**
ΔWS (m s^{-1})	-0.10 ± 1.21	-0.08 ± 0.83	0.54 ± 1.39	1.74 ± 2.32	< 0.01**
ΔPBLH (m)	3.56 ± 178.15	-14.44 ± 139.19	102.41 ± 216.82	156.22 ± 274.82	< 0.01**
ΔU^* (m s^{-1})	-0.01 ± 0.09	-0.01 ± 0.07	0.06 ± 0.10	0.11 ± 0.17	< 0.01**

Note: Data are presented as Mean ± Standard Deviation. The anomalies (Δ) were calculated relative to their respective monthly nocturnal means. The p-values are derived from One-Way ANOVA tests indicating statistical significance under the four weather types.

Text S1: Concentration weighted trajectory (CWT) analysis.

The concentration weighted trajectory (CWT) analysis method quantifies the distribution of pollutant concentrations by calculating the weighted average concentration of air mass trajectories, providing a visual representation of pollution levels (Shi et al., 2024; Zhang et al., 2024). The calculation formula is as follows:

$$C_{ij} = \frac{\sum_{l=1}^{M} C_l \cdot \tau_{ijl}}{\sum_{l=1}^{M} \tau_{ijl}} \quad (1)$$

where C_{ij} represents the average weighted concentration on grid (i,j), C_l is the pollutant concentration corresponding to the trajectory passing through grid (i,j), and τ_{ijl} is the residence time of the trajectory in the grid. To reduce uncertainty, a weighting coefficient is introduced, and the corrected value is denoted as WCWT (Zhang et al., 2024; Wang et al., 2024b). The calculation formula is as follows:

$$WCWT = C_{ij} \times W_{ij} \quad (2)$$

where W_{ij} is the weighting coefficient with specific values (Wang et al., 2024):

$$W_{ij} = \begin{cases} 1.00, & n > 80 \\ 0.70, & 20 < n \leq 80 \\ 0.42, & 10 < n \leq 20 \\ 0.05, & n \leq 10 \end{cases} \quad (3)$$

where n represents the number of trajectories in the grid.

Text S2: Quantitative grouping criteria.

(1) A-type (Anticyclonic group): This category quantitatively lumps all subtypes characterized by strong anticyclonic vorticity and positive SLP anomalies dominating the North China Plain (e.g., Pure A, and hybrid A types like AE, AW). Physically, these are unified by their shared capacity to induce broad regional subsidence.

(2) C-type (Cyclonic group): This lumps subtypes dominated by cyclonic vorticity and negative SLP anomalies (e.g., Pure C, and hybrid C types), unifying them through their shared dynamic triggering of localized convective downdrafts or atmospheric instability.

(3) S-type (Southerly group) & WNE-type (West-North-East group): The directional types were categorized quantitatively based on the dominant azimuth of the geostrophic wind vectors and the strong orientation of the pressure gradient force, representing distinct horizontal advection and shear-induced mixing profiles.

Text S3: Cross-seasonal dynamical consistency of weather types.

To demonstrate that the dynamical mechanisms driving NOI under a specific synoptic classification remain functionally consistent across different seasons, a seasonal stratification analysis was conducted for S-type (Fig. S6).

(1) Horizontal synoptic forcing: As shown in Figs. S6(a) and (b), both spring and autumn S-type are driven by a virtually identical synoptic pressure gradient: lower SLP to the west and a prominent high-pressure system to the east. This forces a robust, seasonally-consistent southerly airflow directly through the study region. The spatial pattern of forcing is fundamentally unchanged.

(2) Vertical structure of motion: Vertically, Figs. S6(c) and (d) confirm a highly consistent structure of vertical motion. In both spring and autumn, the region around Xinxiang is dominated by a prominent upward motion ($\omega < 0$).

(3) Consistency check: The only discernible difference is in the intensity. This verification definitively proves that the overarching physical triggers are functionally comparable across seasons under S-type.

References

Shi, J., Wu, X., Han, X., Zhong, Y., Wang, Z., and Ning, P.: Characterization and sources of carbonaceous aerosols in southwest plateau of China: Effects of biomass burning and low oxygen concentration, Atmos. Environ., 318, 120250, https://doi.org/10.1016/j.atmosenv.2023.120250, 2024.

Wang, H., Qiu, J., Liu, Y., Fan, Q., Lu, X., Zhang, Y., Wu, K., Shen, A., Xu, Y., Jin, Y., Zhu, Y., Sun, J., Wang, H.: MEIAT-CMAQ: A Modular Emission Inventory Allocation Tool for Community Multiscale Air Quality Model, Atmos. Environ., 331, 120604, https://doi.org/10.1016/j.atmosenv.2024.120604, 2024a.

Wang, G., Liu, X., Kong, F., Zhu, Z., Yan, P., Gao, W., and Zhao, N.: Characteristics of fine particulate matter in Linyi during the 24th Olympic winter Games: An insight into the components, sources, transport pathways, and source distribution, Atmos. Pollut. Res., 15, 102034, https://doi.org/10.1016/j.apr.2023.102034, 2024b.

Zhang, L., Yang, L., Kashiwakura, K., Zhao, L., Chen, L., Han, C., Nagao, S., and Tang, N.: Autumn and spring observations of $PM_{2.5}$-bound polycyclic aromatic hydrocarbons and nitro-polycyclic aromatic hydrocarbons in China and Japan, Environ. Pollut., 343, 123139, https://doi.org/10.1016/j.envpol.2023.123139, 2024.